FISEVIER

Contents lists available at ScienceDirect

Journal of Volcanology and Geothermal Research

journal homepage: www.elsevier.com/locate/jvolgeores



Ground-coupled airwaves template match detection using broadband seismic records of explosive eruptions at Popocatépetl volcano, Mexico



Gerardo Mendo-Pérez ^{a,*}, Alejandra Arciniega-Ceballos ^b, Robin S. Matoza ^{c,*}, Alejandro Rosado-Fuentes ^a, Richard W. Sanderson ^c, Bernard A. Chouet ^d

- ^a Posgrado en Ciencias de la Tierra, Universidad Nacional Autónoma de México, Mexico City, Mexico
- ^b Departamento de Vulcanología, Instituto de Geofísica, Universidad Nacional Autónoma de México, Mexico
- ^c Department of Earth Science and Earth Research Institute, University of California, Santa Barbara, CA, USA
- d Arzier-Le Muids, Switzerland

ARTICLE INFO

Article history: Received 27 April 2021 Received in revised form 25 July 2021 Accepted 6 August 2021 Available online 12 August 2021

Keywords:
Template matching
Correlation coefficients
Ground-coupled airwaves
Broadband seismic data
Infrasound
Popocatépetl volcano

ABSTRACT

The utility of infrasound technology for detecting explosive eruptions is well established. However, many active volcanoes are currently monitored exclusively with seismic networks and lack infrasonic sensor networks. Here, we demonstrate the ability of template matching to automatically detect ground-coupled airwave signatures (infrasound signals recorded on seismometers), associated with mild to large explosive eruptions in continuous broadband displacement waveforms from Popocatépetl volcano, Mexico. As templates, we use five verified highamplitude ground-coupled airwave signals that were recorded in November 2017 by both a temporary broadband infrasound array co-located with a broadband seismometer at station ATLI (15.8 km range) and a permanent broadband seismic monitoring station PPIG (4.9 km range). We systematically apply the template matching procedure to two years of continuous seismic records from PPIG station (2017-2018), to identify ground-coupled airwaves in a time span exceeding the operation time of the temporary infrasound array at ATLI. We identify 43 ground-coupled airwaves that occurred during the period of study and with absolute correlation coefficients of $0.5 \le |R| < 0.8$ (using templates of 100 s length). These events are in the catalog of Popocatépetl seismic activity reported by the Centro Nacional de Prevención de Desastres (CENAPRED). The results obtained with template matching using a small number of starting templates points to a ground-coupled airwave signature dominated by a repetitive and fairly stable seismo-acoustic explosion signature during the two-year time frame considered. Future work with an expanded number of templates should improve the results.

© 2021 Published by Elsevier B.V.

1. Introduction

Volcanic infrasound captures shallow and subaerial volcanic processes and complements seismic observations, which primarily reflect subsurface volcanic processes (McNutt, 2000; Chouet, 2003; Fee and Matoza, 2013; Chouet and Matoza, 2013; Matoza et al., 2019b). Although the majority of active volcanoes lack infrasound or acoustic monitoring networks, ground-coupled airwaves have been observed in seismic data from many volcanoes around the world (e.g., Braun and Ripepe, 1993; Ripepe et al., 2001; Ruiz et al., 2006; Johnson and Malone, 2007; De Angelis et al., 2012; Matoza and Fee, 2014; Fee et al., 2016; Smith et al., 2016; Matoza et al., 2018; Haney et al., 2020; lezzi et al., 2020).

Popocatépetl (5452 m.a.s.l.) and Volcán de Fuego. Colima are the most active volcanoes in Mexico. Following Popocatépetl reawakening in 1994 after 70 years of dormancy (De la Cruz-Reyna and Siebe, 1997), its activity has been characterized by recurring gas and ash emissions, and explosive activity. In spite of its location (60 km from Mexico City) and eruptive activity, few investigations have been carried out of the seismo-acoustic wave fields radiated by activity at Popocatépetl. Using seismic data, Zobin et al. (2009) described Popocatépetl explosions in terms of their energy and time delay between a pre-eruptive phase and emissions of ash and pyroclastic materials, documented in videos. Arámbula-Mendoza et al. (2013) observed infrasound signals in the 1-5 Hz band, at distances of 4.8 and 8.4 km from the summit vent and also quantified the ratios of acoustic to seismic energies. Recently, Matoza et al. (2019a) characterized the acoustic wave field radiated by Popocatépetl explosions using a high-broadband and high dynamic range (0.01–100 Hz; ± 500 Pa) infrasound array co-located with a compact broadband seismometer sensor at station ATLI,

^{*} Corresponding authors.

E-mail addresses: gmendoperez@ciencias.unam.mx, gmendoperez@gmail.com
(G. Mendo-Pérez), rmatoza@ucsb.edu (R.S. Matoza).

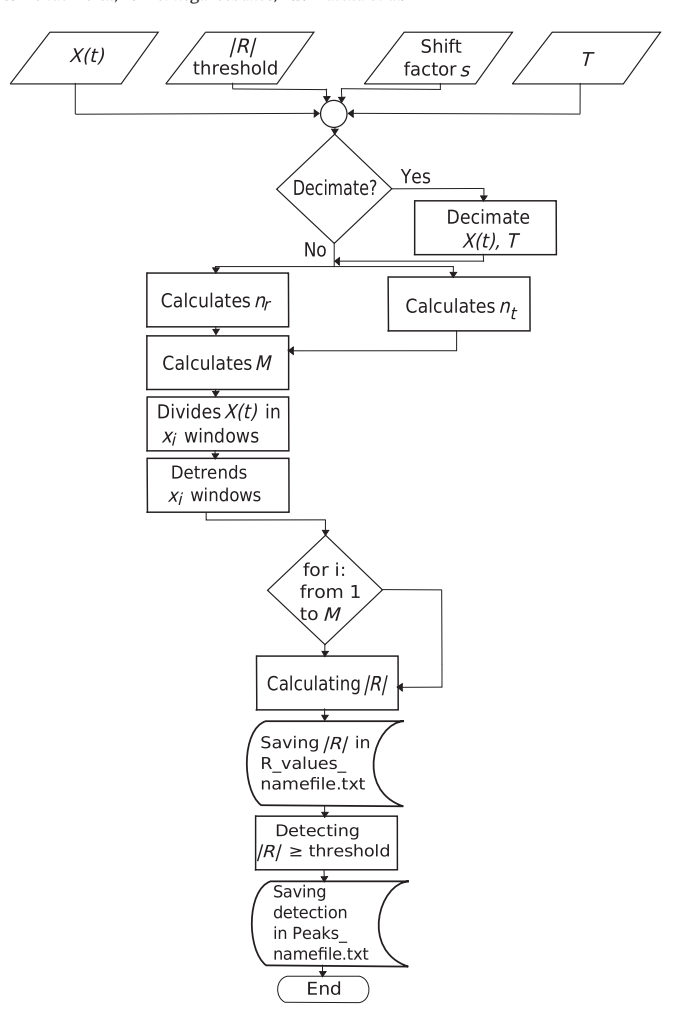


Fig. 1. Flow chart of the Automatic Template Matching Code (ATMC) that detects ground-coupled airwaves. X(t) represents the seismogram to be analyzed in the search for airwaves that match a template T. |R| is the threshold value of the absolute normalized correlation coefficient, s is the overlapping factor, in samples, between x_i and T, n_t is the number of samples of T, n_t is the number of samples of T, n_t is the number of samples of T, T, is divided.

identifying high-amplitude ground-coupled airwave signatures in Popocatépetl broadband seismograms.

Here we assess the feasibility of detecting infrasound explosion signatures by template matching with seismic data only, using two full years of data (2017 and 2018) from the permanent Popocatépetl seismic station, PPIG. For this purpose, we developed an Automatic Template Matching Code (hereafter named ATMC) to systematically detect ground-coupled airwaves in broadband seismograms. As templates, we used displacement waveforms recorded at PPIG associated with verified ground-coupled airwaves identified at ATLI during an overlapping data period of these stations in November 2017.

2. Template matching

Cross-correlation and template matching are widely utilized in seismic data processing to evaluate the similarity between waveforms and events of interest (Stephens and Chouet, 2001; Gibbons and Ringdal, 2006; Shelly et al., 2007; Brown et al., 2008; Shelly and Hill, 2011; Matoza et al., 2015; Skoumal et al., 2015; Lengliné et al., 2016). Template matching utilizes the correlation coefficient between a master/template signal and equal-length records extracted from seismograms of interest. Following Gubbins (2004) and Gibbons and Ringdal (2006), the cross-correlation between two discrete time signals is given by:

$$S_{XT} = \sum_{i=0}^{n_t} (x_i \cdot T) \tag{1}$$

where S_{XT} is the cross-correlation function, T is the template, x_i is the i-th time window extracted from the seismic record X(t), and n_t is the number of samples. The number of samples in both T and x_i must be equal.

Using Eq. (1), the normalized correlation coefficient, *R*, is given by:

$$R = \frac{S_{XT}}{\sqrt{S_{XX}S_{TT}}} \tag{2}$$

where S_{XX} is the autocorrelation of X(t), S_{TT} is the autocorrelation of T, and S_{XT} is the cross-correlation of x_i and T obtained using Eq. (1). The degree of similarity between x_i and T is evaluated in the range of the correlation coefficient $-1 \le R \le 1$. The closer T is to T or T, the higher the degree of similarity between T and T. Values of T close to

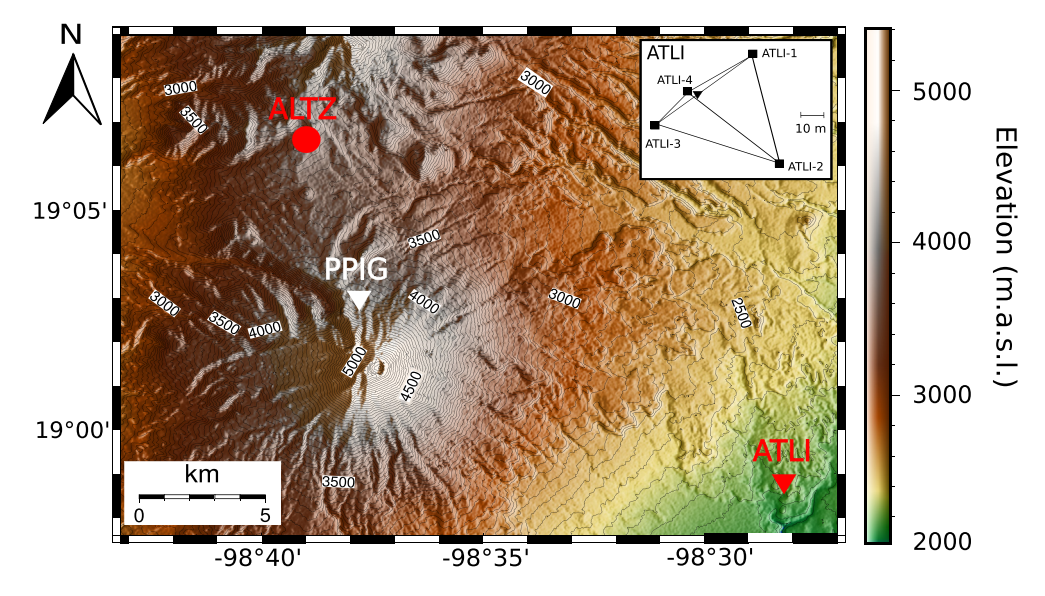


Fig. 2. Popocatépetl topography map and the locations of PPIG seismic station (white triangle), operated by the Servicio Sismológico Nacional, UNAM, the temporary infrasound array ATLI (red triangle) (September 2017–June 2018), and the meteorological station Altzomoni (red solid circle) operated by the Red Universitaria de Observatorios Atmosféricos (RUOA, https://www.ruoa.unam.mx). ATLI geometry is showed in the upper right corner. Contour lines are every 50 m. (For interpretation of the references to color in this figure legend, the reader is referred to the web version of this article.)

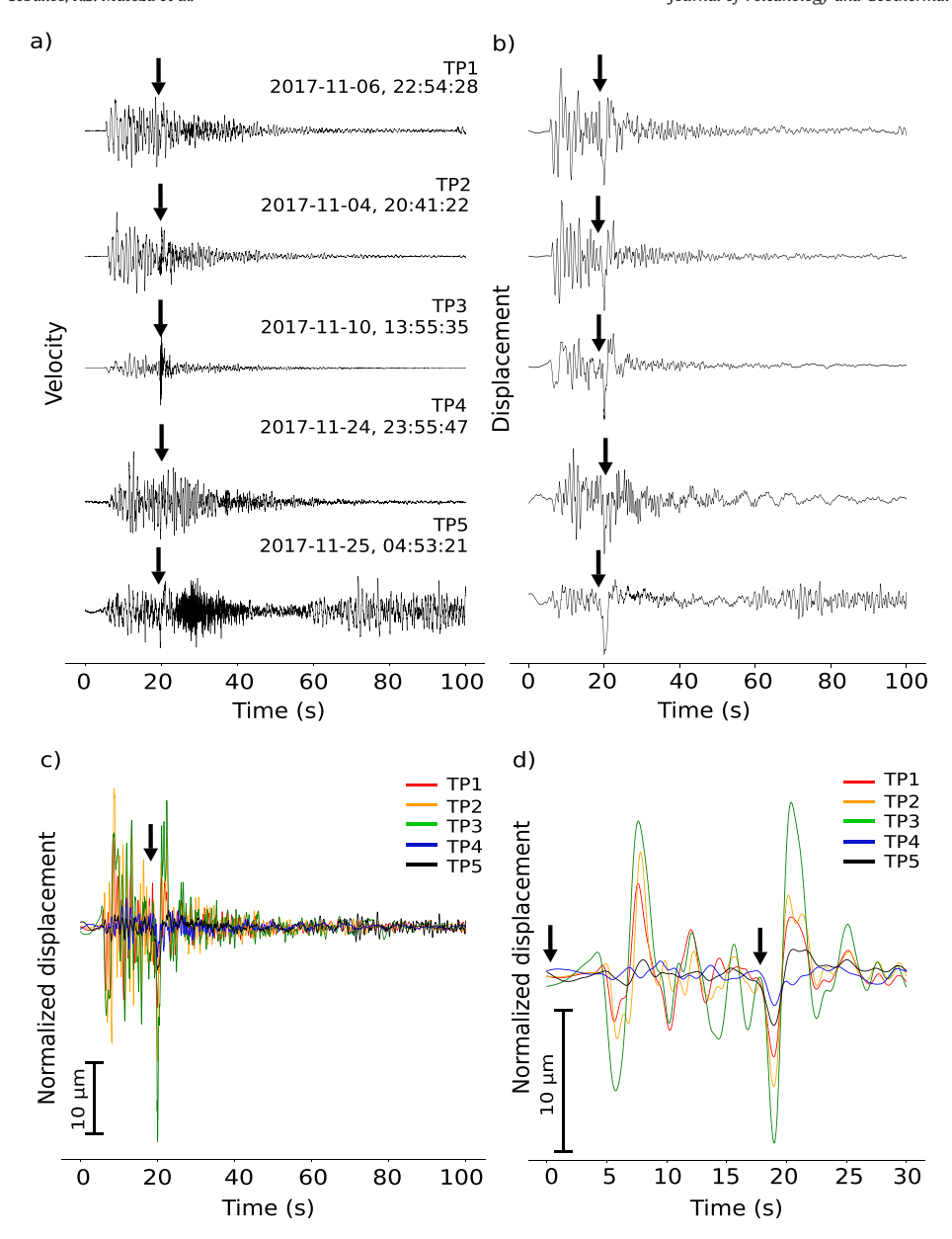


Fig. 3. Templates traces retrieved from PPIG seismograms. Normalized vertical component of velocity a) and displacement b). Name, date and UTC time of each template are indicated at the right. Time in x-axis are with respect to the origin time of the events. For amplitude comparison, displacement templates are overlapped in c). Traces and names are distinguished by colors. d) Seismic and air phase signals are displayed after band-pass filtering in 0.01–0.5 Hz. The arrows indicate the onset of the seismic and the air phases. All traces were corrected for instrument response. (For interpretation of the references to color in this figure legend, the reader is referred to the web version of this article.)

zero indicate a lack of similarity between x_i and T_i . Negative values of R imply inverse correlation.

The ATMC calculates R by systematically applying template matching using the logic in the flow chart shown in Fig. 1. The ATMC counts a detection using a threshold value representing the minimum correlation coefficient imposed by the analyst. All data are first deconvolved for instrument response. The input data are the threshold value, the continuous displacement records X(t), the template T and an overlapping shift factor S between S windows. Each seismogram S divided into S time windows, with each S0 sharing the same sampling rate and number of samples as the template S1 i.e.,

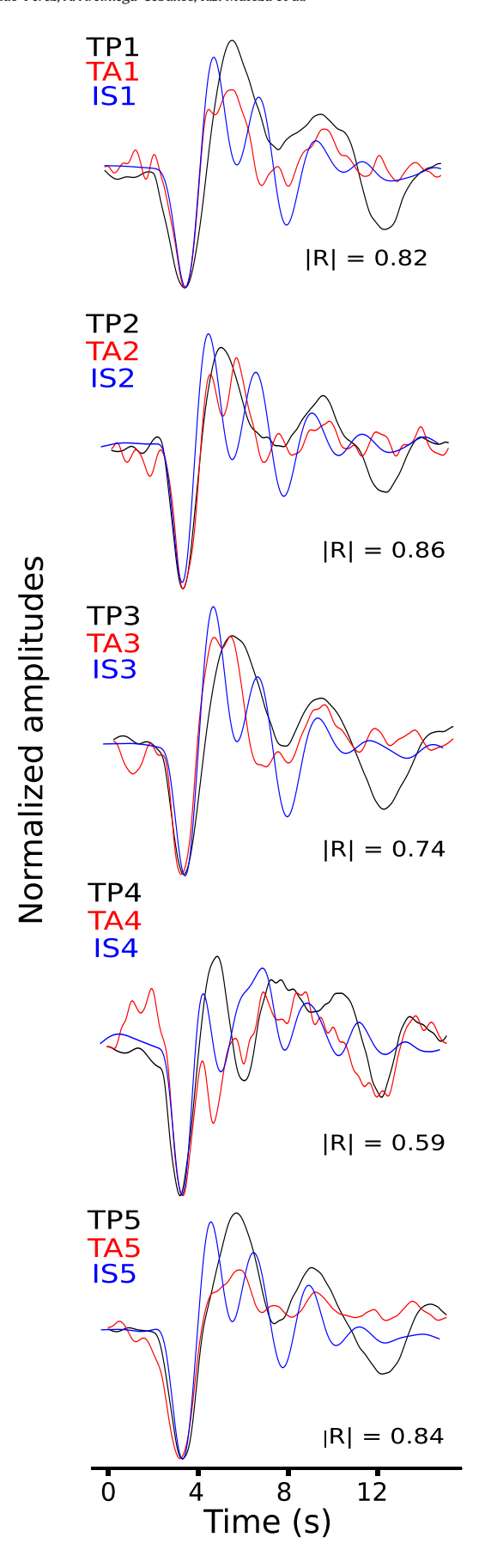
$$M = \frac{s}{n_{\star}}(n_r - n_t) + 1 \tag{3}$$

where n_r the number of samples in X(t), n_t denotes the number of samples in the template, and s = 1, 2, 3, ... is the shift factor.

The ATMC generates a matrix A_{MxN} representing M windows by N samples, and calculates the absolute correlation coefficient |R| for each window (Eq. (2)). To distinguish between detections and noise, ATMC uses a peak finding routine to detect amplitude changes with respect to a threshold (Duarte and Watanabe, 2018), and |R| values below the specified threshold are rejected.

3. Templates and PPIG data

Popocatépetl volcano is monitored by the Centro Nacional de Prevención de Desastres (CENAPRED) and the Servicio Sismológico Nacional (SSN) of the Instituto de Geofísica, Universidad Nacional Autónoma de México (UNAM). PPIG is one of the SSN stations used for regional seismicity and volcano surveillance and is equipped with a Streckeisen STS-2 seismometer and a 24-bit Quanterra Q330S+digitizer. PPIG is located at 4000 m.a.s.l. (19.066° N, —98.628° W),



4.9 km N of the summit vent (Fig. 2). We retrieved both ground-coupled airwaves and seismic signals from PPIG continuous vertical displacement records (at 100 samples per second (sps)) from 2017 to 2018 (SSN. 2017).

The templates used to detect ground-coupled airwaves at PPIG were identified using recorded displacement waveforms at PPIG associated with infrasound airwaves of explosions recorded by the ATLI array in November 2017 (Fig. 2). The ATLI ground-coupled airwaves were used to identify and compare PPIG templates but not to run the ATMC. ATLI featured four high-broadband acoustic sensors (Hyperion IFS-3111) and one broadband seismic sensor (120-s Trillium Compact Posthole). All sensors have flat response ~0.01–100 Hz and were separated approximately 50 m in a triangle-shaped array with the seismic sensor at the center of the array (Fig. 2). ATLI was deployed 15.8 km ESE of Popocatépetl summit during a temporary seismo-acoustic experiment (Matoza et al., 2019a).

Using the date and time of the ground-coupled airwaves identified at the ATLI broadband seismometer, we retrieved the corresponding displacement signals from the PPIG seismograms and selected five events associated with mild explosions (Figs. 3 and 4). Fig. 3a and b show the velocity and displacement records, respectively, of the five templates recorded at PPIG. These events named TP1 to TP5 (for PPIG templates), contain the ground-coupled airwaves depicted in Fig. 3c, which are normalized displacement waveforms superimposed for comparison. To emphasize the seismic and air phases in these templates, we applied a band-pass filter (0.01-0.5 Hz) and overlapped 30 s long windows (Fig. 3d). In addition, to compare air phases recorded at PPIG and ATLI we extracted and normalized, from infrasound records and seismograms at ATLI (named TA1 to TA5) and displacement waveforms at PPIG, the phases associated with the ground-coupled airwaves and superimposed them in Fig. 4, after filtering in the 0.01–0.5 Hz band. The filtering is just for comparison, input data to run ATMC were not filtered. Note that the events recorded at PPIG contain similar waveforms to those recorded at the ATLI seismic receiver (Fig. 4).

We calculate the correlation coefficient |R| between these signals (e.g., TA1 vs TP1, TA2 vs TP2, and so on) to have a reference of similarity. All |R| are above or equal to 0.74, with the exception of TA4 vs TP4, where |R|=0.59. The maximum amplitude displacements of TP1, TP2 and TP3 airwaves have peak-to-trough values of 18.34 μ m, 30.04 μ m, and 48.8 μ m, respectively. These values are at least twice the maximum peak-to-trough amplitudes at ATLI, where TA1, TA2 and TA3 show displacements of 8.05 μ m, 11.87 μ m, and 7.8 μ m, respectively. These differences are in agreement with wave propagation considering the distances from the Popocatépetl vent to PPIG and ATLI (Fig. 2).

We can confirm these amplitudes through a comparison of the intensity values between PPIG and ATLI events in terms of their energy density as:

$$U_e = \frac{\rho}{d} \int_0^d |v(t)|^2 dt \tag{4}$$

where v(t) is the velocity record in m/s, d is the event duration in seconds (100 s), and ρ is the mass density of the medium in kg/m³. As the seismometers at PPIG and ATLI are deployed on comparable composition soils, taking into account the range of density of Popocatépetl deposits

Fig. 4. Comparison of displacement waveforms retrieved from PPIG (black lines) and ATLI (red lines) seismograms associated with the air phases recorded by the infrasound sensor ATLI-4 (blue lines). These traces are normalized and band-pass filtered (0.01–0.5 Hz); the name of the template and the absolute normalized cross-correlation coefficient value |R| obtained between PPIG and ATLI are indicated in each plot. (For interpretation of the references to color in this figure legend, the reader is referred to the web version of this article.)

Table 1

Name of each template for PPIG and ATLI. Date (yyyy-mm-dd) and time, with respect to PPIG, of the explosive events used as templates. Energy density per event and site calculated using Eq. (4) and a template window length (event duration) of 100 s. The normalized correlation coefficient values |R| obtained between PPIG templates (for details see Section 4).

Site		Date & time (UTC)	Energy density (µJ/m³)		Normalized absolute correlation coefficient R				
PPIG	ATLI		PPIG	ATLI	TP1	TP2	TP3	TP4	TP5
TP1	TA1	2017-11-04, 20:41:22	12.00	0.69	1.00	0.73	0.69	0.28	0.43
TP2	TA2	2017-11-06, 22:54:28	30.50	1.41	0.73	1.00	0.65	0.34	0.38
TP3	TA3	2017-11-10, 13:55:35	41.70	2.18	0.69	0.65	1.00	0.30	0.49
TP4	TA4	2017-11-24, 23:55:47	2.09	0.47	0.28	0.34	0.30	1.00	0.31
TP5	TA5	2017-11-25, 04:53:21	1.35	0.15	0.43	0.38	0.49	0.31	1.00

spanning 900 kg/m³ for pumices to 2600 kg/m³ for juvenile lithics (Arana-Salinas et al., 2010), we may assume that an average density of 1750 kg/m³ provides reasonable energy estimates. The energy densities for the analyzed events are listed in Table 1. For these calculations, we use a duration of 100 s (both seismic and airwave phases). Observe that in PPIG and ATLI, TP3 and TA3 are the most energetic signals where the ground-coupled airwave energy dominates in both velocity and displacement records (Fig. 3a and b), while TP5 and TA5 are the signals with lowest energy. The energy ratios between the templates of PPIG relative to

ATLI are 17.39, 21.63, 19.12, 4.44, and 9.00, yielding an average of 14.31 (Table 1). These energy differences, as well as the peak-to-trough values between PPIG and ATLI, are partially explained by geometrical spreading and distances of these stations from the volcano vent (see Fig. 2). Local site effects cannot be ruled out, however, to fully quantify these effects would require further studies that are beyond the purpose of this work.

We calculated |R| between each PPIG template in order to identify waveform differences. Observe that although the templates present a clear ground-coupled air phase, they do not present the same waveform specifically in the seismic phase (see Fig. 3). The |R| values between TP1, TP2, and TP3 range between 0.65 and 0.73, indicating a high degree of waveform similarity (Table 1). On the contrary, for TP4 and TP5, |R| barely reaches 0.35, indicating that there is little similarity between these signals, nor with respect to TP1, TP2, or TP3. The lack of similarity between TP1, TP4, and TP5 (see Table 1) suggests that these events represent different explosive mechanisms and, therefore, we selected these events to run ATMC over the two years of seismic data. We discuss the effects in finding detections due to the template waveform differences in Section 6.

Events TP1, TP2, and TP3 are described in CENAPRED Popocatépetl activity reports (http://www.cenapred.unam.mx/reportesVolcanGobMX/) as "high energetic explosive events that lofted columns into the atmosphere up to heights exceeding 2 km above the summit", while TP4 and TP5 are both referred to as "explosive volcanic activity with sustained degassing". Those descriptions are not meant to differentiate the type of

Table 2List of the 43 events detected by ATMC in PPIG records using templates TP1, TP2 and TP3: number of event, date (yyyy-mm-dd), UTC and local times, correlation coefficient $|R| \ge 0.5$, and the description of Popocatépetl eruptive events reported in CENAPRED catalog (http://www.cenapred.unam.mx/reportesVolcanGobMX/). All these events correspond to Category 1 (see Section 6). Events with an asterisk corresponds to TP1, TP2 and TP3.

No.	Event date	Event time (UTC)	Event time (Local time)	<i>R</i>	Description of activity by CENAPRED
E1	2017-01-24	19:18:00	13:18:00	0.54	1 explosion. Low content of ash fall-out.
E2	2017-05-07	14:05:00	09:08:00	0.55	12 explosions. Emissions of gas, ash and water
E3	2017-10-05	07:26:00	02:26:00	0.60	5 explosions. Volcanic tremor two hours after explosions.
E4	2017-10-05	11:42:00	06:42:00	0.59	5 explosions. Volcanic tremor two hours after explosions.
E5	2017-10-05	19:31:00	14:31:00	0.53	5 explosions. Volcanic tremor two hours after explosions.
E6	2017-10-06	13:22:00	08:22:00	0.58	4 explosions. Light ash fall-out.
E7	2017-10-07	01:13:00	20:13:00	0.52	3 explosions, 2 explosions with ash column height less than 2000 and 3000 m.
E8	2017-10-07	05:49:00	00:49:00	0.67	3 explosions, 2 explosions with ash column less than 2000 m and 3000 m of heigh
E9	2017-10-08	19:28:00	14:28:00	0.65	4 explosions
E10	2017-10-09	03:14:00	22:14:00	0.53	4 explosions. One reported previous day.
E11	2017-10-09	20:27:00	15:27:00	0.56	4 explosions. One reported previous day.
E12	2017-10-10	06:26:00	01:26:00	0.72	4 explosions.
E13	2017-10-10	08:14:00	03:14:00	0.73	4 explosions.
E14	2017-10-11	04:48:00	23:48:00	0.70	2 explosions. No visibility to the volcano.
E15*	2017-11-04	20:40:00	14:40:00	1.00	3 explosions.
E16*	2017-11-06	22:53:00	16:53:00	0.73	1 explosion. Ash column of 2500 m of height
E17*	2017-11-10	13:34:00	07:34:00	0.69	3 explosions. Ash column of 3000 m of height.
E18	2018-30-01	22:21:00	16:21:00	0.59	4 explosions. Light ash fall-out.
E19	2018-07-19	03:36:00	22:36:00	0.52	1 explosion.
E20	2018-07-19	04:31:00	23:31:00	0.63	1 explosion.
E21	2018-07-19	02:30:00	21:30:00	0.61	6 explosions. Light ash fall-out.
E22	2018-07-19	16:00:00	11:00:00	0.50	6 explosions. Light ash fall-out.
E23	2018-09-18	17:48:00	12.48:00	0.73	8 explosions. 204 min of harmonic tremor.
E24	2018-09-23	01:00:00	20:23:00	0.68	5 explosions.
E25	2018-09-25	08:18:00	03:18:00	0.72	11 explosions.
E26	2018-09-29	07:10:00	02:10:00	0.56	4 explosions.
E27	2018-10-07	16:19:00	11:19:00	0.70	5 explosions.
E28	2018-10-07	22:20:00	17:20:00	0.53	5 explosions
E29	2018-11-28	18:57:00	12:57:00	0.51	1 explosion.
E30	2018-11-28	02:02:00	20:02:00	0.54	1 explosion.
E31	2018-12-02	15:22:00	09:22:00	0.54	4 explosions. Two with ash column heights of 1500 and 2500 m.
E32	2018-12-04	08:30:00	02:30:00	0.53	2 explosions, Emission of material.
E33	2018-12-04	16:56:00	10:56:00	0.50	2 explosions. Emission of material.
E34	2018-12-07	12:46:00	06:46:00	0.55	2 explosions. Ash column height of 1800 m.
E35	2018-12-08	04:44:00	22:44:00	0.55	3 explosions. Two with ash column heights of 1500 and 2000 m.
E36	2018-12-08	05:22:00	23:22:00	0.62	3 explosions. Two with ash column heights of 1500 and 2000 m.
E37	2018-12-08	18:27:00	12:27:00	0.61	3 explosions. Two with ash column heights of 1500 and 2000 m.
E38	2018-12-09	07:39:00	01:39:00	0.73	4 explosions. Three with ash column heights of 1500, 2500 and 3000 m.
E39	2018-12-09	13:51:00	07:51:00	0.71	4 explosions. Three with ash column heights of 1500, 2500 and 3000 m.
E40	2018-12-09	16:35:00	10:35:00	0.64	4 explosions. Three with ash column heights of 1500, 2500 and 3000 m.
E41	2018-12-10	12:49:00	06:49:00	0.66	2 explosions. One with ash colum height of 1100 m.
E42	2018-12-10	17:43:00	11:45:00	0.55	2 explosions. One with ash colum height of 1100 m.
E43	2018-12-16	00:58:00	18:58:00	0.71	5 explosions. Detected by TP5.

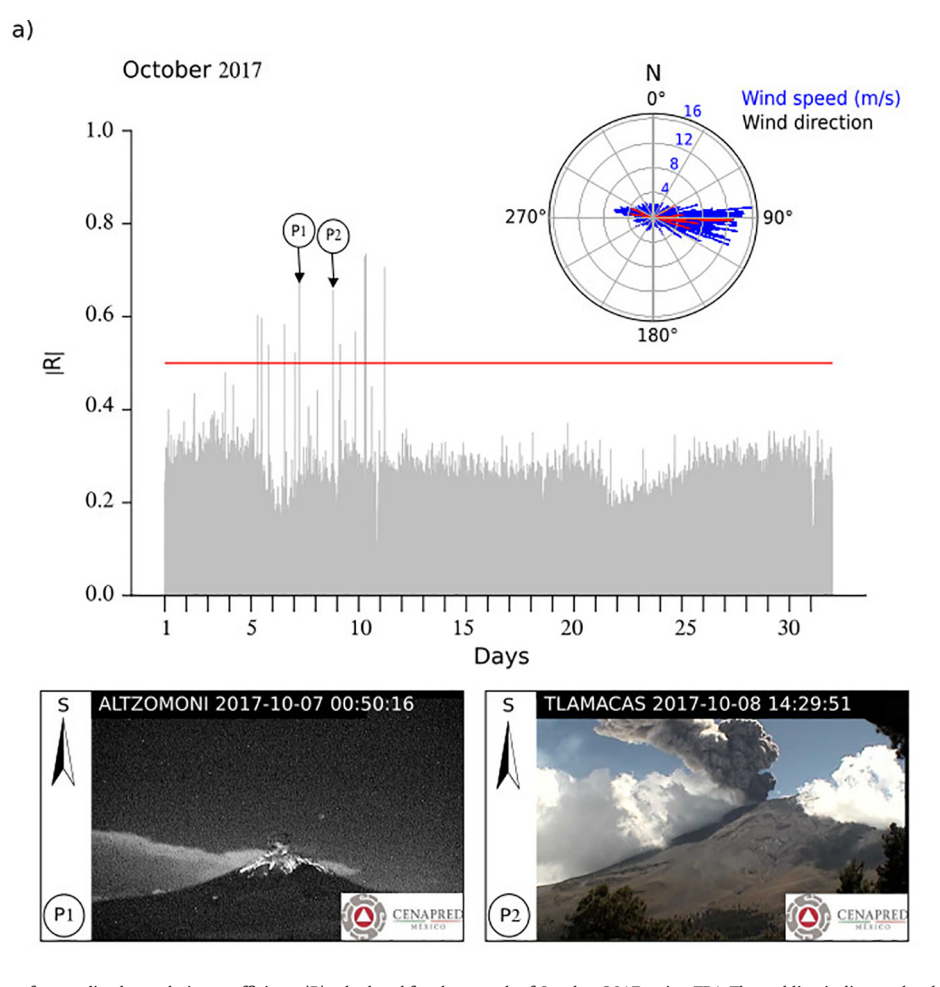


Fig. 5. a) Example of time-series of normalized correlation coefficients |R| calculated for the month of October 2017, using TP1. The red line indicates the threshold value. The polar plot shows wind direction (black) and wind speed (blue) relative to Altzomoni station. Detected events are highlighted in red. Wind data was taken from Altzomoni RUOA webpage (https://www.ruoa.unam.mx). Images illustrate the type of eruption for events occurred on 2017-10-07, 05:50:16 UTC and on 2017-10-07, 19:29:51 UTC, denoted by P1 and P2 respectively. The arrow shows the direction where the camera points to. These images were taken from the CENAPRED webpage (http://cenapred.unam.mx/reportesVolcanGobMx/). b) Same as in Fig. 5a, for December 2018. Images P3 and P4 correspond to events that occurred on 2018-12-08, 18:29:21 UTC and 2018-10-09, 19:39:42 UTC, respectively. (For interpretation of the references to color in this figure legend, the reader is referred to the web version of this article.)

activity associated with the templates. In fact, explosive events with clear seismic and infrasonic phases are the main characteristics of the templates. These features distinguish the events that CENAPRED reports since the catalog counts many types of emissions. Therefore, the events that ATMC searches for are those mild to large explosion where the acoustic waveform is clearly distinguishable in seismic displacement records (denoted by arrows in Fig. 3a and b). For this reason, the number of events reported in CENAPRED catalog cannot be compared directly with the results obtained with ATMC. On the other hand, we set the minimum |R| threshold to declare a match at 0.5, given that ATMC is looking for mild to large explosive events in PPIG seismograms, which are affected by wind as well as electronic noise from a TV transmitter station located less than 1 km away.

4. Results

4.1. Detected events

The dominant vertical interaction between the atmosphere and the ground makes ground-coupled airwaves easier to recognize in the PPIG vertical displacement component than in horizontal records. In addition, ground-coupled airwave signals show up as negative pulses on vertical displacement seismograms, indicating that they are anti-correlated with the infrasound records due to grazing

incidence (Ben-Menahem and Singh, 1981; de Groot-Hedlin and Hedlin, 2019; Matoza et al., 2019a). The ground-coupled airwaves are not detected in the horizontal components or these airwaves are weak, therefore we restricted our analysis to the vertical component.

Table 2 lists events detected by ATMC that present seismic and air phases and are reported by CENAPRED. The table includes only the dates and number of events reported by CENAPRED of those days when ATMC detected an explosion with seismic and air phases that matched any of the characteristics of TP1, TP2 and TP3 templates (Fig. 3a-d). Using TP1, we detected 43 ground-coupled airwaves in PPIG data from 2017 to 2018, including TP2 and TP3 (Table 2). Their associated |R| range between 0.5 and 0.8. Fig. 5a and b show examples of | R| for October 2017 and December 2018, along with the respective polar plot of wind direction and wind speed, and photographs documenting typical eruptive activity during these months. Observe that the dominant wind direction pattern was quite regular. This suggests that neither the wind direction nor its velocity (ranging between 0.8 m/s and 16 m/ s) affected the waveform characteristics of the explosions. Therefore, we may consider that our results are independent of wind conditions. The polar plots are obtained using data from the Altzomoni meteorological station, located 6.4 km 20° NW from PPIG (Fig. 2), and is part of the Red Universitaria de Observatorios Atmosféricos (https://www.ruoa. unam.mx).

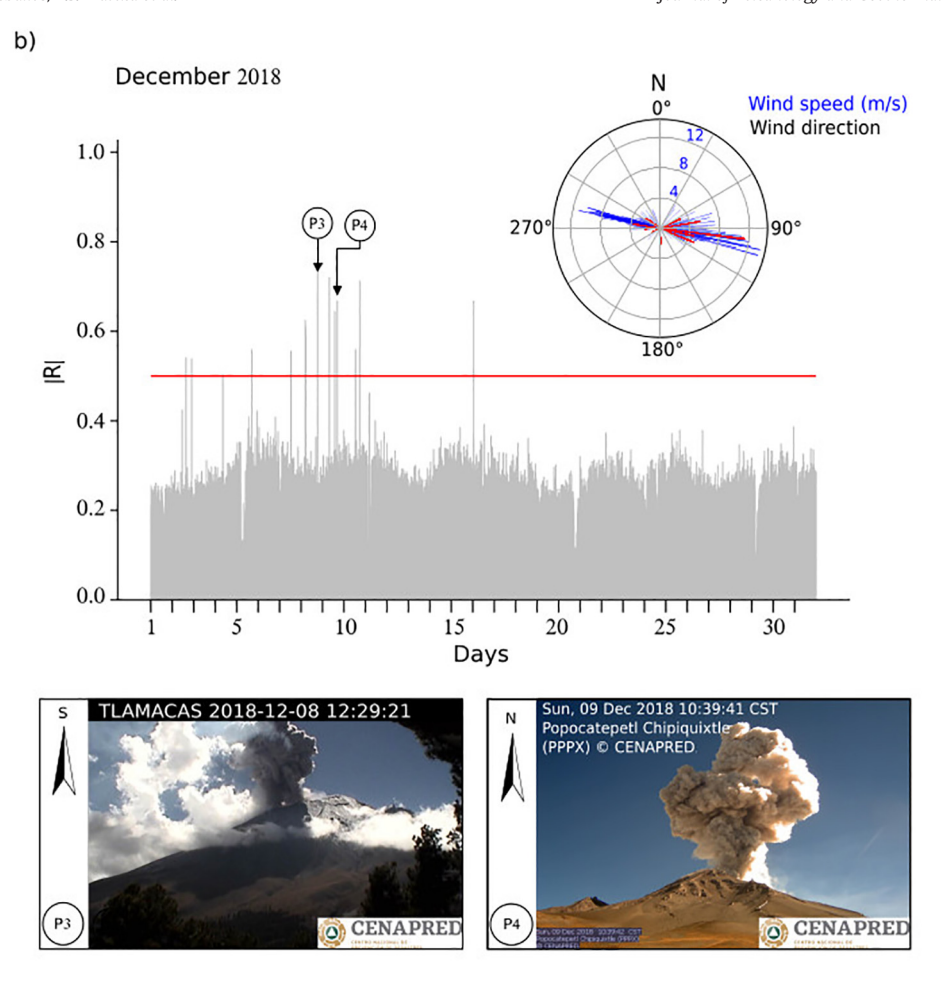


Fig. 5 (continued).

For the two years of analyzed data, the values of |R| plotted in Fig. 5a and b do not present any trend with time. The lowest rates of ground-coupled airwaves occurred in January and May 2018 (additional |R| plots can be found in the supplementary material). For TP4 no detections were found and for TP5 only one event was detected (see Table 2). This implies that TP4 and TP5 were rare events during the study interval. Furthermore, the low intensity characteristics of such events made their airwave signals difficult to detect at PPIG (Fig. 3a and d).

The waveforms of the 43 detected events (17 events detected in 2017, 26 events detected in 2018) are stacked for comparison with TP1 (see Fig. 6a and b). In order to emphasize the seismic and air phases, we calculate the |R| value over a 50 s time window between the stack and original signal. The |R| between the stack and TP1 is 0.90, with minor discrepancies concentrated in the time window before the airwave appears and in the last 10 s of the record. The stack and TP1 were band-pass filtered from 0.01 Hz and 0.5 Hz (Fig. 6c).

4.2. Travel-times interpretation

Fig. 7a shows the maximum displacement amplitude $|U_{max}|$ versus the corresponding travel time difference, t_{ap} – t_{sp} , where t_{ap} is the arrival time of the airwave phase and t_{sp} is the arrival time of the seismic phase. For all events, $|U_{max}|$ is the peak-to-trough value of each airwave detected using TP1. Fig. 7b shows examples of how t_{ap} and t_{sp} are measured in the displacement traces after filtered in the 0.01–0.5 Hz band to obtain accurate travel times. Most of the delays in Fig. 7a are concentrated between 12 s and 14 s (with only one erratic

delay at 18 s), standard deviation of t_{ap} – t_{sp} with respect to the average is 1 s and with respect to TP1 is 1.31 s. Similar travel time delays (11–16 s) were recorded by a receiver located 4.6 km from the vent of Tungurahua volcano in Ecuador (Ruiz et al., 2006). No obvious trend between t_{ap} – t_{sp} and $|U_{max}|$ is apparent, and the amplitude $|U_{max}|$ variations, of about two orders of magnitude, suggest stability in their origin. Therefore, to interpret these travel time delays we estimate the velocity of acoustic waves both in the atmosphere around the Popocatépetl region and in the conduit. Additionally, we estimate the P-wave velocity for shallow depths (<5 km) and assume two relative simple scenarios: 1) the medium is homogenous having constant velocity and 2) the medium is heterogenous with a constant velocity gradient with depth (Beydoun and Ben-Menahem, 1985; Sánchez-Sesma et al., 2001).

For the first scenario, we take a P-wave velocity of 3.5 km/s for shallow depths (< 5 km), which is consistent with the velocity model used to locate Popocatépetl volcanic events using seismic networks (Valdes et al., 1995; Arciniega-Ceballos et al., 2000, 2008) and has been validated by waveform inversion models of long-period and very-long period signals related to mild explosions (Chouet et al., 2005; Arciniega-Ceballos et al., 2012). Moreover, given that the predominant periods (1–2 s) of events shown in Fig. 7a, are related to large wavelengths, lateral heterogeneities can be neglected. Therefore, for such a homogenous medium the seismic phase would arrive at PPIG in $^{H}t_{p}=1.40$ s.

Delving into the second assumption, the curved ray travel time for the seismic phase (τ) , that features the constant velocity gradient medium for which the velocity is $V_p(z) = V_p(z_r)(1 + (z-z_r)/h)$, can be

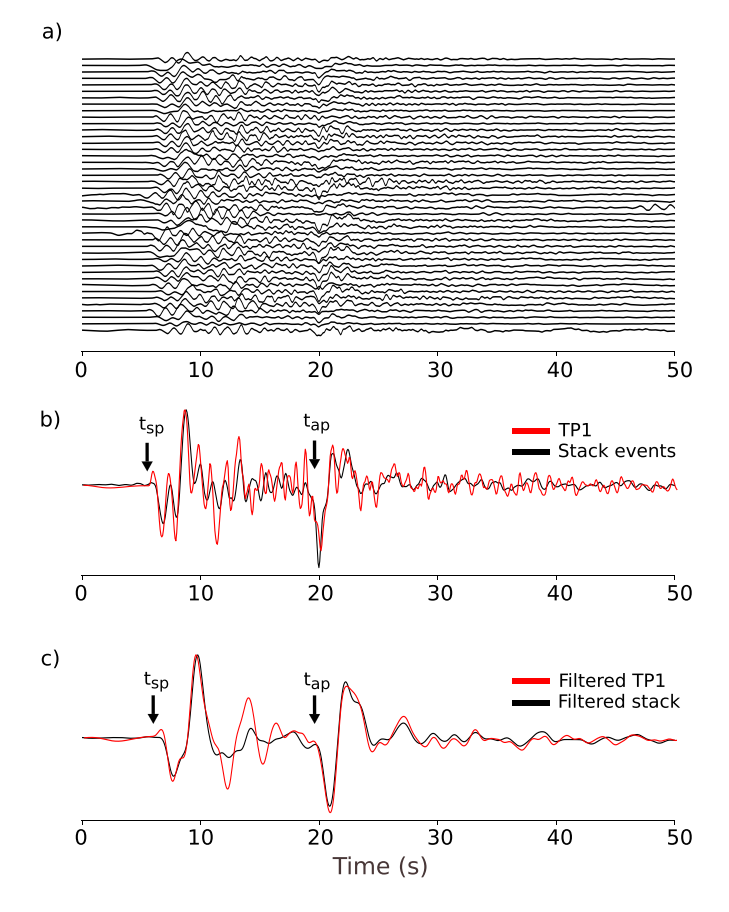


Fig. 6. a) Traces of the 43 detected events ($|R| \ge 0.5$) from 2017-01-01 to 2018-12-31 using TP1. b) Stack of detected events (black line) compared with the waveform of TP1 (red line). The |R| between these two waveforms is 0.90. In c) are displayed the waveforms shown in (b) after filtering in the 0.01-0.5 Hz band to emphasize the air phase and facilitate time picking and comparison. The arrows in b) and c) point to the arrival times of the seismic phase (t_{sp}) and to the ground-coupled air phase (t_{ap}) . Amplitudes in all traces are normalized with respect to their maximum. (For interpretation of the references to color in this figure legend, the reader is referred to the web version of this article.)

obtained following Beydoun and Ben-Menahem (1985) and Sánchez-Sesma et al. (2001) as:

$$\tau = [Vp(z_r)/h]^{-1} \ln\left(\frac{R_2 + R_1}{R_2 - R_1}\right)$$
 (5)

where $Vp(z_r)/h$ is the velocity gradient, h is a length between the level of zero velocity and the level $z = z_r$ of the reference wave velocity $Vp(z - z_r)$, taken as 540 m/s (Fig. 8b).

Here, $R_1 = \sqrt{x^2 + (z - z_r - z_0)^2}$ is the distance between the source and the observation point at (x, z), z_0 is the source depth and $R_2 =$

 $\sqrt{x^2+(z+(z_r-z_0)+2h)^2}$ is the distance between an image source of a bipolar reference system at depth $-(z_0+2h)$ and the observation point. The wave paths depend on the take-off angles; shallower sources (< 200 m depth) may feature impossible ray paths towards PPIG, and deeper sources (\ge 200 m) take-off downward and accelerate with depth drifting vertically away from the station. Eq. (5) is computed for the depth interval 0 to 800 m every 20 m (Fig. 8a), estimating the velocity gradient (V_p (z_r/h)) taking the derivative from the velocity curve show in Fig. 8b. This curve was obtained using the basaltic andesitic model for shallow structures (< 500 m) in volcanoes (Lesage et al., 2018). For larger depths ($500 \le z < 800$ m) we assigned 3.5 km/s. Finally, the average travel-time to PPIG is $^Gt_p = 1.22$ s, under the state conditions.

Additionally, the propagation velocity of acoustic waves can be obtained from the effective sound speed equation (Bass et al., 1991; Garcés et al., 1998; Fee and Matoza, 2013):

$$c_{eff} = \sqrt{\gamma R_g T_g} + \hat{n} \cdot \mathbf{u} \tag{6}$$

where \boldsymbol{u} is the wind velocity in the direction given by the unit vector \hat{n} . The air constant $R_g = 286 \,\mathrm{m}^2/\mathrm{s}^2/\mathrm{K}$, the specific heat ratio $\gamma = 1.4$, and T_g is temperature in Kelvin. We estimate $c_{eff} = 338 \,\mathrm{m/s}$ using the average values for the wind speed (5 m/s) and temperature (278.15 K) at an altitude of 4000 m.a.s.l. (these values are obtained from the web site of the Altzomoni meteorological station; https://www.ruoa.unam.mx/index.php?page=estaciones&id=2).

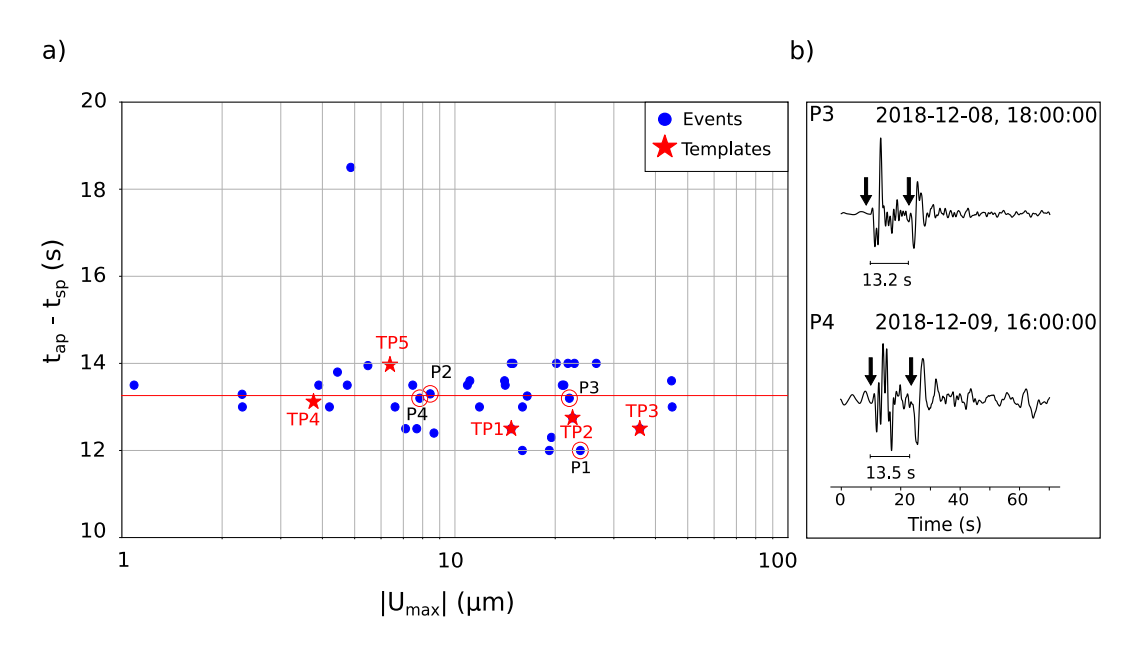


Fig. 7. a) The maximum displacements amplitudes |Umax| of detected events shown in Fig. 6a, using TP1 versus the arrival times difference between the seismic phase (t_{sp}) and the air phase (t_{ap}) (blue dots). Red stars indicate templates TP1 to TP5. The red line shows the mean value of the arrival time differences. Events in red circles correspond to the images of the eruptions shown in Fig. 5a and b. The signals P3 and P4 filtered in 0.01–0.5 Hz band, depicted in panel b) exemplify the picking of arrival times (indicated by the arrows) to calculate the seismic and air phases time differences. (For interpretation of the references to color in this figure legend, the reader is referred to the web version of this article.)

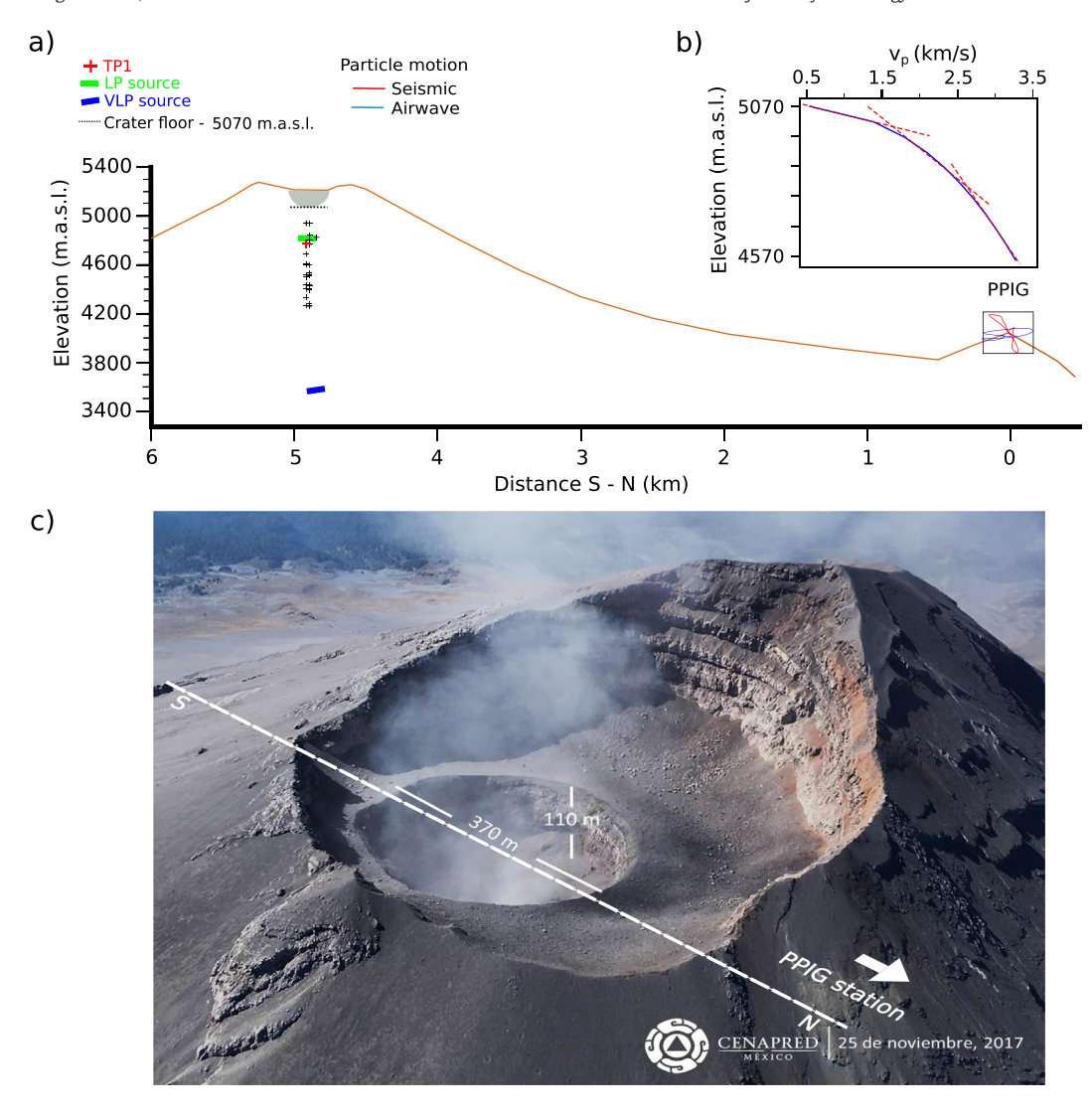


Fig. 8. a) S-N profile of Popocatépetl volcano (in red) using the view of the crater taken from the photograph (http://cenapred.unam.mx/reportesVolcanGobMx/) and elevation data points from Google Earth. Plotted at PPIG station is the particle motion of template TP1 for seismic (red line) and air wave (blue line) phases. The grey shaded area indicates the crater floor. Black crosses indicate the seismic source region inferred using time differences t_{ap} - t_{sp} of the events displayed in Fig. 7a. The blue rectangles indicate the centroid location of LP and VLP seismic sources (Arciniega-Ceballos et al., 2012). b) Velocity curve calculated every 20 m, using the basaltic andesitic model for shallow structures in volcanoes (blue solid line) (Lesage et al., 2018). Red dashed lines indicate the velocity gradient. See Section 5 for details. (For interpretation of the references to color in this figure legend, the reader is referred to the web version of this article.)

Taking the line of sight between PPIG and the Popocatépetl summit we find that the acoustic phase (t_{ap}) would reach PPIG in ~15.0 s assuming linear propagation. Besides this part of travel time in the atmospheric path, we add the travel time inside the conduit assuming that the source mechanism consists of a pressurized conduit that explodes at z_0 emitting mixtures of gas, ash and other volcanic materials, at average velocities of 130–160 m/s (Alatorre-Ibargüengoitia and Delgado-Granados, 2006; Alatorre-Ibargüengoitia et al., 2011). In this scenario, the acoustic waves travel faster than the volcanic materials, which are driven by gas expansion (Alatorre-Ibargüengoitia et al., 2011; Arciniega-Ceballos et al., 2015). Then, as the characteristics of the conduit (geometry, filling material, etc.), are unknown and may affect considerably the wave velocity, we assumed that the conduit is clear and that the acoustic waves travel in the range from Mach 1 to Mach 6 (Tameguri et al., 2002; Yamada et al., 2016).

Therefore, the average travel times considering vertical paths from depths 50–800 m to the vent, for Mach 1 is $^{M1}t_c=1.17$ s and for Mach 6 is $^{M6}t_c=0.19$ s.

Adding these values to the travel time from the vent to PPIG (t_{ap} = 15.0 s) and subtracting the P-wave travel times, ${}^{H}t_{p}$ = 1.40 s and ${}^{G}t_{p}$ = 1.22 s, respectively, we can obtain the average delays related to the

whole path. For the homogeneous medium ($^{M1H}t_a$ - $^{H}t_p$ = 14.8 s and $^{M6H}t_a$ - $^{H}t_p$ = 13.8 s) and for the constant-gradient velocity medium ($^{M1G}t_a$ - $^{G}t_p$ = 15.0 s and $^{M6G}t_a$ - $^{G}t_p$ = 14.0 s). The depth range for the events shown in Fig. 7a, as first approximation with respect to PPIG elevation Z_{PPIG} (4000 m.a.s.l.), can be estimated as $Z = c_{eff}(t_{ap}-t_{sp}+{}^{M6}t_c)-Z_{PPIG}$, yielding 130 to 810 m (Fig. 8a). These results suggest that regardless of the P-wave velocity assumptions, the higher the acoustic velocity in the conduit is, the better constrained the data is.

Particle trajectories of displacement in the horizontal and vertical planes obtained in the 0.01–0.5 Hz band for TP1 and the stack of the 43 events are shown in Fig. 9a and b. According to Neuberg and Pointer (2000), the topography correction applies for shallower sources than half of the wavelength of the dominant frequency of the signal. For PPIG it can be neglected given the dominant period range of 1–10 s and the wavelengths involved using 3500 km/s for the first 5 km (Valdes et al., 1995; Arciniega-Ceballos et al., 2000, 2008).

Then, particle motion was calculated for the specific time window related to the seismic and the air phases. The patterns of the particle motion in the horizontal plane for the seismic phases (Fig. 9a and b) point directly to the volcano and the air phases roughly coincide

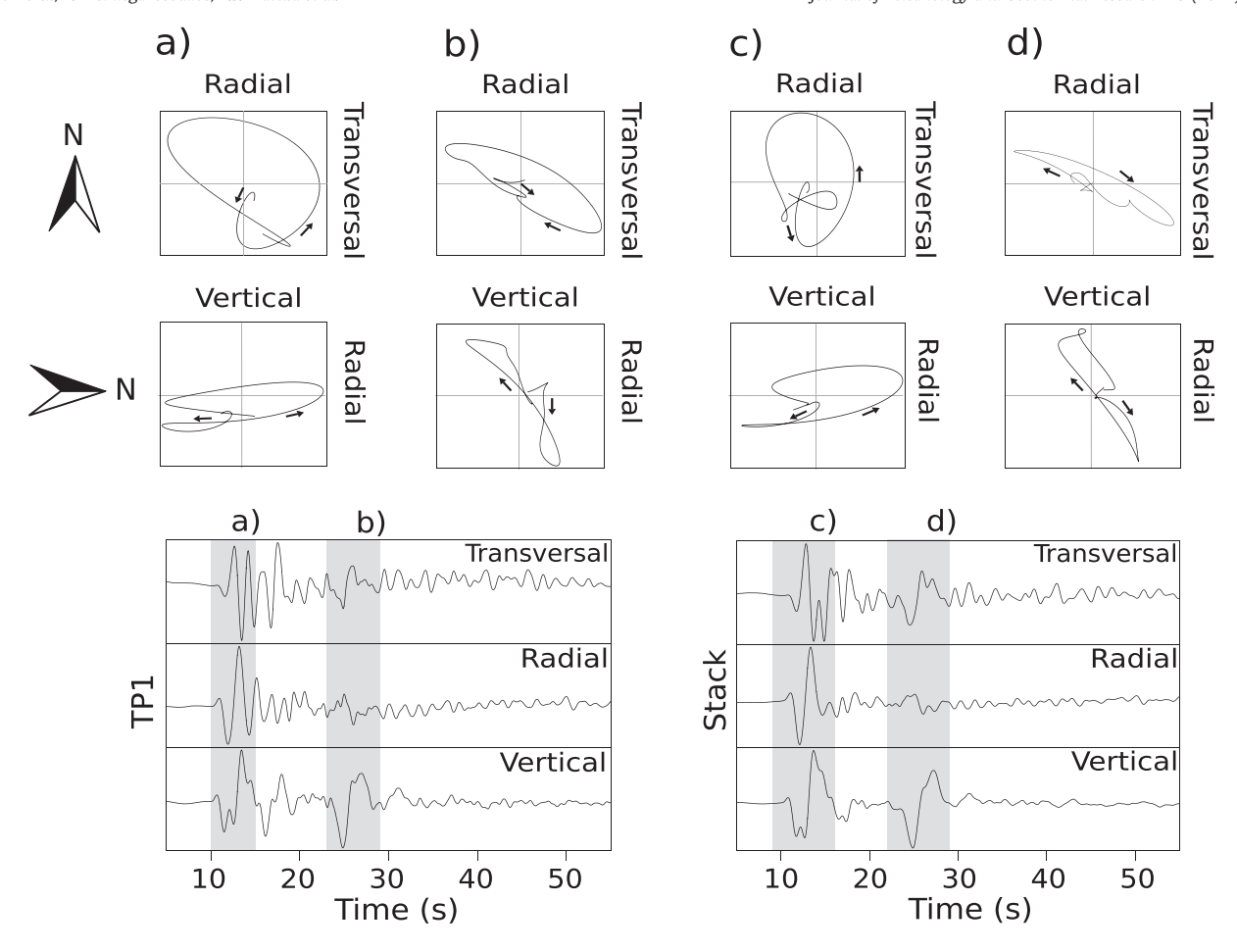


Fig. 9. Trajectories of particle motion in the horizontal (radial-transversal) and vertical (vertical-radial) planes; top and middle panels, respectively. Shaded bars in each bottom panel indicate the time window used in the particle motion plots for the seismic and the airwave phases; a) and b) respectively, for template TP1, and c) and d), respectively, for the stack of detected events. The arrows indicate the direction of motion. Seismic traces are filtered in the 0.01–0.5 Hz frequency band.

with the wind direction (NW-SE) that predominated during the period of study (see polar plots in Fig. 5a and b and supplemental material). Therefore $c_{\it eff} = 338$ m/s is adequate for our calculations. Note that the particle motion in the vertical plane suggests that seismic waves arrive to PPIG from depth with an acute angle (Fig.9a and 9b).

5. Discussion

In summary, the common characteristics of detected events are: (1) similar waveforms (see Figs. 3, 7b); (2) travel time differences t_{ap} $t_{\rm sp}$ near 13.4 s (see Fig. 7a); and (3) comparable events representative of mild explosions with eruptive column heights ranging from 500 m to 3000 m above the summit (Fig. 5a and b, Table 2). These similarities suggest that these events share similar mechanisms and originate from a restricted source region that was active at least during the period of study (2017–2018). The 2 s travel time variation between the seismic and the air phases indicates a proportional variation in source depth. The extended source region may range between 130 and 800 m depth below the vent (Fig. 8a). This estimation coincides with the distribution of hypocenters for longperiod events (Arciniega-Ceballos et al., 2008) and falls within the region constrained by centroid depth locations imaged from waveform inversion of very-long-period signals (1500 m) and long-period signals (± 250 m) recorded at Popocatépetl volcano (Arciniega-Ceballos et al., 1999, 2012; Chouet et al., 2005). Similar interpretations of infrasound and seismic records were used to locate the seismic source regions at Stromboli volcano (Braun and Ripepe, 1993; Ripepe et al., 2001), Tungurahua (Ruiz et al., 2006), and Mt. Cleveland (De Angelis et al., 2012; Iezzi et al., 2020).

We first set the |R| threshold to 0.5 but we noticed that small degassing events could also be detected using a lower threshold value of 0.4. However, selecting lower threshold values $(0.4 \le |R| < 0.5)$ involves more human intervention requiring a careful selection of time windows to eliminate tremor and earthquakes, and to identify events hidden in microseismic noise and rejecting false detections. ATMC could be adapted to consider smaller volcanic events but here we target moderate to large explosions. Therefore, to exemplify detected versus undetected events, event traces are organized in three categories in Fig. 10a-c. The first category includes detected events using TP1, whose |R| are in the range 0.5–0.8. These events were reported by CENAPRED and present clear air phase (Fig. 10a). Waveform characteristics of these events coincide with those of long-period events classified as Type I by Arciniega-Ceballos et al. (2008). To confirm the number of successful detections running TP1 we ran ATMC with templates TP2 and TP3 and obtained the same 43 detected events (see Table 2). The second category covers events with $0.4 \le |R| < 0.5$ (a total of 38 events) using templates TP1 and TP2. These events are also reported in the CENAPRED catalog. Note that for these events, the signal that would correspond to the arrival time of the air phase is unclear due to their small amplitudes and masking influence of microseismicity (see Fig. 10b). This happens because ATMC takes into account the whole template length (100 s) comprising seismic and air phases. Therefore, the events in category 2 (Fig. 10b) are examples where the detection is dominated by the seismic phase. This indicates that although not all explosive events contain a recognizable air phase, these can be detected by ATMC. The third category exemplifies some of the events reported by CENAPRED that ATMC did not detect. Note that these events are buried in microseismicity noise and require filtering above 1 Hz to become

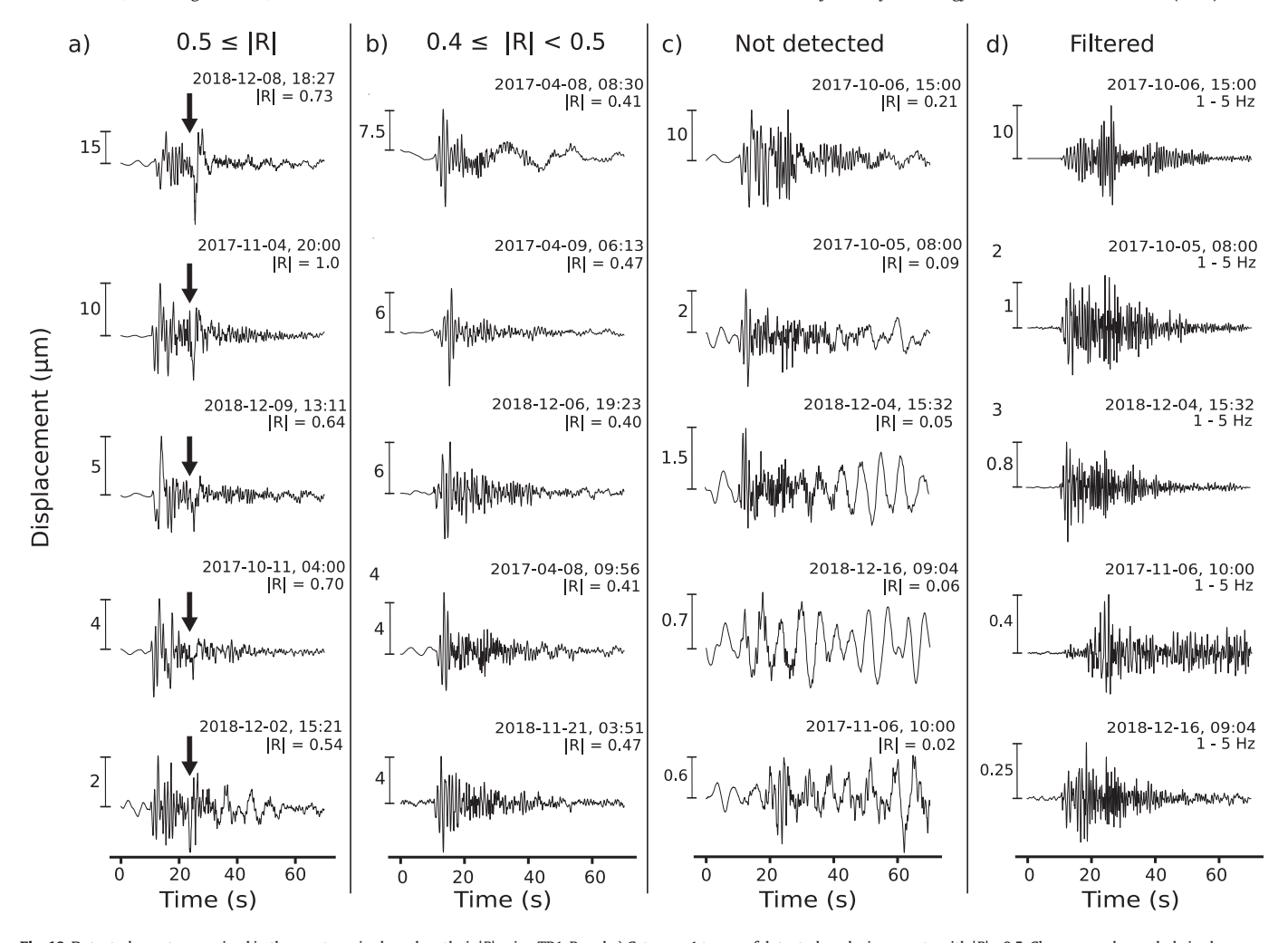


Fig. 10. Detected events organized in three categories based on their |R| using TP1. Panel a) Category 1 traces of detected explosive events with $|R| \ge 0.5$. Clear ground-coupled air phases can be observed and are indicated by black arrows. Panel b) Category 2 examples of detected events with $0.4 \le |R| < 0.5$. Panel c) Category 3 traces of undetected events by ATMC but reported by CENAPRED. Panel d) depicts the signals shown in panel c) after high-pass filtered (1 Hz). Time and date in UTC and |R| of each event are at the upper right of plot. The size of the bars at the left side of each plot, represents the maximum peak-to-though amplitude relative to the scale bar in the y-axes (see Section 5 for major explanation).

visible (see examples of these signals in Fig. 10c and d). These signals do not contain seismic or air phases that can categorize them as explosive events.

Microseismic noise in and around Popocatépetl features dominant periods between 2 and 12 s, which may also range up to 20 s (Arciniega-Ceballos et al., 1999, 2003). When the amplitude ratio between the volcanic signal to microseismic noise is low, the only recourse to retrieve the volcanic signals is by filtering the seismic record, the point is that the filtered signals are not mild or large explosive events. The filtering may affect the airwave dominant frequency (0.4 Hz) since it is close to the microseismicity frequency range (Matoza et al., 2019a). Therefore, we tested several time windows in order to find the window length for which ATMC detects more events and eliminate the codas where microseismic noise may be predominant. We ran ATMC using 10 s, 20 s, 30 s, 40 s, 50 s template windows and compare the results with 100 s window. To exemplify these calculations, we randomly selected two records 24 h long; 2017-04-23 (Julian day 113) and 2018-12-08 (Julian day 342). For 2017-04-23, we obtained a total of 268 detections for 10 s window, 28 detections for 20 s window, 1 detection for 30 s window, and no detections from 40 s, 50 s and 100 s. For 10 s, 20 s and 30 s most of the detections are false positives, thus these window lengths are discarded.

On the other hand, for 2018-12-08 we obtained 2131 detections with 10 s window and 247 detections for 20 s window, all of which are false positives. For the 30 s, 3 of 6 detections are false. Finally, for

40 s, 50 s and 100 s windows only 3 detections were found which coincide with those detected by TP1. However, comparing 40 s, 50 s and 100 s, using TP2, TP3, TP4 and TP5 as well, although ATMC runs 12 to 25% faster with 40 s and 50 s than 100 s, with 40 s and 50 s ATMC generates a huge amount of false positives. For 40 s and 50 s TP1 and TP2 yielded consistently the same results with 100 s for events in categories 1 and 2 (see Fig. 10a and b). In contrast, although TP3 detected the events listed in categories 1 and 2, it produced hundreds of false positive detections related to microseismic noise and surfaces waveforms unrelated to volcanic airwaves. Using TP4, ATMC did not detect any event, and using TP5, ATMC detected some of the events in category 1, however at the cost of thousands of false detections. Templates present high similarity, their slight differences prone each template to detect the seismic or air wave phases predominantly. Therefore, for the analysis we used 100 s window length for the templates TP1, TP2, TP3, TP4 and TP5.

6. Conclusions

In this work we described an Automatic Template-Matching Code (ATMC) to systematically identify volcanic explosions recorded as ground-coupled airwaves in broadband seismograms. We analyzed two years of continuous broadband seismic records from the permanent PPIG seismic station of Popocatépetl. We used five templates of 100 s length identified at PPIG associated with waveforms of

ground-coupled airwaves recorded at ATLI (Figs. 3 and 4). Running ATMC with templates TP1, TP2 and TP3, we found 43 events with |R| in the range 0.5–0.8, these events are reported by CENAPRED (Table 2).

Our results indicate that a correlation coefficient above 0.5 is sufficient to identify explosive events and their associated ground-coupled airwaves in displacement seismograms. The activity during the period of study was dominated by repeated events associated with mild degassing explosions sharing similar waveforms as templates TP1, TP2, and TP3, and displaying a wide range of amplitudes (Figs. 3, 7 and 10). Amplitude intensities can be related to initial pressure conditions that drives seismic and acoustic sources, which for a simple interpretation could be at depths 130-800 m below the crater floor of Popocatépetl (Figs. 7 and 8). These results suggest that Popocatépetl has maintained a degree of non-destructive source mechanism through 2017–2018, consistent with observations since its reawakening in 1994 (Arciniega-Ceballos et al., 1999, 2012, 2015; Chouet et al., 2005). However, not all explosive events produced by Popocatépetl present a repetitive character and, therefore, these may not be detected by a template matching procedure using a handful of templates. Nevertheless, to confirm the above observations, our current work includes the identification of signals related to ground-coupled airwaves in seismograms recorded in broadband seismic networks using recent and past data. A next step in this research will be a detailed investigation of the effects of infrasound propagation variability and wind noise (e.g., Matoza and Fee, 2018; Matoza et al., 2019b; and references therein) on the ATMC capabilities to enable the detection of different types of explosions and ground-coupled airwaves around Popocatépetl.

ATMC would be enhanced by increasing the template library, enabling the identification and classification of different explosive signatures associated with the evolution of Popocatépetl explosive behavior, thereby improving hazards assessment.

Online material

The Python code including an example is at the Github repository: https://github.com/GerardoMendo/ATMC

Open software and data statement

ATMC is available in Github (https://github.com/GerardoMendo/ATMC) and can be adapted to different types of seismic records. In this work, ATMC processed 48 months of seismic data, divided in records of one-hour long each at 14 sps, in approximately 48 h. The code ran on Debian 10 Buster using Linux 19.0 and Python 3.7, using an Intel I5 2.8 GHz, 8 Gb in RAM and 512 Gb SSD computer.

All data from the temporary station ATLI are available at the IRIS Data Management Center (DMC): (Matoza and Arciniega-Ceballos, 2017). Popocatépetl Volcano Temporary Deployment, 2017–2018 [Data set]. International Federation of Digital Seismograph Networks, http://www.fdsn.org/networks/detail/5K_2017/. All data from the PPIG station are available at the Servicio Sismológico Nacional, Instituto de Geofísica, Universidad Nacional Autónoma de México (http://www.ssn.unam.mx).

Authors contribution

Gerardo Mendo-Pérez compiled data, wrote the code, performed analysis, co-created and worked on the figures, drafted the manuscript and reviewed the manuscript critically.

Alejandra Arciniega-Ceballos directed the research, drafted the manuscript, conducted analysis, co-created and worked on the figures, reviewed the manuscript criti-cally and directed revisions.

Robin S. Matoza directed the research and reviewed the manuscript critically.

Richard W. Sanderson reviewed the manuscript critically. Alejandro Rosado-Fuentes reviewed the manuscript critically. Bernard A. Chouet reviewed the manuscript critically.

Funding

This work was funded by grants from Universidad Nacional Autónoma de México (UNAM), DGAPA-PAPIIT IN105716; IN108219 and by Consejo Nacional de Ciencia y Tecnología (CONACYT) and the University of California Institute for Mexico and the United States (UC MEXUS). RSM and RWS were also funded by NSF grants EAR-1847736 and EAR-1614855. ARF and GMP were supported by CONACYT doctorate scholarship program.

Declaration of Competing Interest

The authors declare that they have no known competing financial interests or personal relationships that could have appeared to influence the work reported in this paper.

Acknowledgements

This work was supported by grants from Universidad Nacional Autónoma de México (UNAM), DGAPA-PAPIIT IN105716; IN108219 and by Consejo Nacional de Ciencia y Tecnología (CONACYT) and the University of California Institute for Mexico and the United States (UC MEXUS). GMMP acknowledges CONACYT and UC MEXUS grant for supporting his academic stay at the UC Santa Barbara. RSM and RWS were also funded by NSF grants EAR-1847736 and EAR-1614855. We thank Antonio Carrillo Ledesma for his technical support and Xvoli Pérez Campos. Data were obtained by the Servicio Sismológico Nacional (México), station maintenance, data acquisition and distribution are thanks to its personnel. Meteorological data were obtained from the Red Universitaria de Observatorios Atmosféricos, UNAM (https:// www.ruoa.unam.mx). We used NumPy (Harris et al., 2020), Scipy (Virtanen et al., 2020), ObsPy (Beyreuther et al., 2010), and Matplotlib (Hunter, 2007) for analyzing and plotting the data. We used The Generic Mapping Tools in the preparation of Fig. 2 (Wessel and Smith, 1991). We thank Oliver Lamb and an anonymous reviewer for their useful comments and the review of the paper.

Appendix A. Supplementary data

Supplementary data to this article can be found online at https://doi.org/10.1016/j.jvolgeores.2021.107378.

References

Alatorre-Ibargüengoitia, M.A., Delgado-Granados, H., 2006. Experimental determination of drag coefficient for volcanic materials: Calibration and application of a model to Popocatépetl volcano (Mexico) ballistic projectiles. Geophys. Res. Lett. 33 (11). https://doi.org/10.1029/2006GL026195.

Alatorre-Ibargüengoitia, M.A., Scheu, B., Dingwell, D., 2011. Influence of the fragmentation process on the dynamics of Vulcanian explosions: an experimental approach. Earth Planet. Sci. Lett. 302, 51–59. https://doi.org/10.1016/j.epsl.2010.11.045.

Arámbula-Mendoza, R., Valdés-González, C., Varley, N., Juárez-García, B., Alonso-Rivera, P., Hernández-Joffre, V., 2013. Observation of Vulcanian explosions with seismic and acoustic data at Popocatépetl Volcano, Mexico. In: Zobin, V.M. (Ed.), Complex monitoring of volcanic activity: Methods and results, 1st ed. Nova Science Publishers, Inc., pp. 13–33.

Arana-Salinas, L., Siebe, C., Macías, J.L., 2010. Dynamics of the ca. 4965 yr ¹⁴C BP "Ochre Pumice" Plinian eruption of Popocatépetl volcano, México. J. Volcanol. Geotherm. Res. 192 (3–4), 212–231. https://doi.org/10.1016/j.jvolgeores.2010.02.022.

Arciniega-Ceballos, A., Chouet, B.A., Dawson, P., 1999. Very long-period signals associated with Vulcanian explosions at Popocatepetl Volcano, Mexico. Geophys. Res. Lett. 26 (19), 3013–3016. https://doi.org/10.1029/1999GL005390.

Arciniega-Ceballos, A., Valdes-Gonzalez, C., Dawson, P., 2000. Temporal and spectral characteristics of seismicity observed at Popocatepetl Volcano, Central Mexico. J. Volcanol. Geotherm. Res. 102 (3–4), 207–216. https://doi.org/10.1016/S0377-0273(00)00188-8.

Arciniega-Ceballos, A., Chouet, B., Dawson, P., 2003. Long-period events and tremor at Popocatepetl volcano (1994 – 2000) and their broadband characteristics. Bull. Volcanol. 65, 124–135. https://doi.org/10.1007/s00445-002-0248-8.

- Arciniega-Ceballos, A., Chouet, B., Dawson, P., Asch, G., 2008, Broadband seismic measurements of degassing activity associated with lava effusion at Popocatépetl Volcano, Mexico. J. Volcanol. Geotherm. Res. 170 (1-2), 12-23. https://doi.org/10.1016/j. ivolgeores 2007 09 007
- Arciniega-Ceballos, A., Dawson, P., Chouet, B.A., 2012. Long period seismic source characterization at Popocatépetl volcano, Mexico. Geophys. Res. Lett. 39 (20). https://doi. org/10 1029/2012GI053494
- Arciniega-Ceballos, A., Alatorre-Ibargüengoitia, M.A., Scheu, B., Dingwell, D.B., 2015, Analysis of source characteristics of experimental gas burst and fragmentation explosions generated by rapid decompression of volcanic rocks. J. Geophys. Res. Solid Earth 120 (7), 5104–5116. https://doi.org/10.1002/2014JB011810.
- Bass, H.E., Bolen, L.N., Raspet, R., McBride, W., Noble, J., 1991. Acoustic propagation through a turbulent atmosphere: Experimental characterization. J. Acoust. Soc. Am. 90 (6), 3307-3313, https://doi.org/10.1121/1.401441.
- Ben-Menahem, A., Singh, S.J., 1981. Seismic Waves and Sources (First Edition). Springer-
- Verlag. Beydoun, W.B., Ben-Menahem, A., 1985. Range of validity of seismic ray and beam methods in general inhomogeneous media — II. A canonical problem. Geophys. J. Int. 82 (2), 235–262. https://doi.org/10.1111/j.1365-246X.1985.tb05136.x.
- Beyreuther, M., Barsch, R., Krischer, L., Megies, T., Behr, Y., Wassermann, J., 2010. ObsPy: a Python Toolbox for Seismology. Seismol. Res. Lett. 81 (3), 530-533. https://doi.org/ 10.1785/gssrl.81.3.530.
- Braun, T., Ripepe, M., 1993. Interaction of seismic and air waves recorded at Stromboli Volcano. Geophys. Res. Lett. 20 (1), 65-68. https://doi.org/10.1029/92GL02543.
- Brown, J.R., Beroza, G.C., Shelly, D.R., 2008. An autocorrelation method to detect low frequency earthquakes within tremor. Geophys. Res. Lett. 35 (16). https://doi.org/10. 1029/2008GL034560.
- Chouet, B., 2003. Volcano seismology. Pure Appl. Geophys. 160, 739-788. https://doi.org/ 10.1007/PL00012556.
- Chouet, B.A., Matoza, R., 2013. A multi-decadal view of seismic methods for detecting precursors of magma movement and eruption. J. Volcanol. Geotherm. Res. 252, 108-175. https://doi.org/10.1016/j.jvolgeores.2012.11.013.
- Chouet, B., Dawson, P., Arciniega-Ceballos, A., 2005. Source mechanism of Vulcanian degassing at Popocatépetl Volcano, Mexico, determined from waveform inversions of very long period signals. J. Geophys. Res. Solid Earth 110 (B7). https://doi.org/10. 1029/2004IB003524.
- De Angelis, S., Fee, D., Haney, M., Schneider, D., 2012. Detecting hidden volcanic explosions from Mt. Cleveland Volcano, Alaska with infrasound and ground-coupled airwaves. Geophys. Res. Lett. 39 (21). https://doi.org/10.1029/2012GL053635.
- de Groot-Hedlin, C., Hedlin, M., 2019. Detection of infrasound signals and sources using a dense seismic network. In: Le Pichon, A., Blanc, E., Hauchecorne, A. (Eds.), Infrasound Monitoring for Atmospheric Studies, 2nd. ed. Springer, Cham, pp. 669-700 https:// doi.org/10.1007/978-3-319-75140-5.
- De la Cruz-Reyna, S., Siebe, C., 1997. The giant Popocatépetl stirs. Nature 388 (227). https://doi.org/10.1038/40749.
- Duarte, M., Watanabe, R.N., 2018. Notes on Scientific Computing for Biomechanics and Motor Control. GitHub repository. https://github.com/BMClab/BMC.
- Fee, D., Matoza, R.S., 2013. An overview of volcano infrasound: from hawaiian to plinian, local to global. J. Volcanol. Geotherm. Res. 249, 123-139. https://doi.org/10.1016/j. jvolgeores.2012.09.002.
- Fee, D., Haney, M., Matoza, R.S., Szuberla, C., Lyons, J., Waythomas, C., 2016. Seismic envelope-based detection and location of ground-coupled airwaves from volcanoes in Alaska. Bull. Seismol. Soc. Am. 106 (3), 1024-1035. https://doi.org/10.1785/
- Garcés, M.A., Hansen, R.A., Lindquist, K.G., 1998. Traveltimes for infrasonic waves propagating in a stratified atmosphere. Geophys. J. Int. 135 (1), 255-263. https://doi.org/ 10.1046/j.1365-246X.1998.00618.x.
- Gibbons, S.J., Ringdal, F., 2006. The detection of low magnitude seismic events using array-based waveform correlation. Geophys. J. Int. 165 (1), 149-166. https://doi. org/10.1111/j.1365-246X.2006.02865.x.
- Gubbins, D., 2004. Time Series Analysis and Inverse Theory for Geophysicists. Cambridge University Press https://doi.org/10.1017/CBO9780511840302.
- Haney, M.M., Fee, D., McKee, K.F., Lyons, J.J., Matoza, R.S., Wech, A.G., Tepp, G., Searcy, C., Mikesell, T.D., 2020. Co-eruptive tremor from Bogoslof volcano: seismic wavefield composition at regional distances. Bull. Volcanol. 82 (18). https://doi.org/10.1007/ s00445-019-1347-0.
- Harris, C.R., Millman, K.J., van der Walt, S.J., Gommers, R., Virtanen, P., Cournapeau, D., Wieser, E., Taylor, J., Berg, S., Smith, N.J., Kern, R., Picus, M., Hoyer, S., van Kerkwijk, M.H., Brett, M., Haldane, A., Fernández del Río, J., Wiebe, M., Peterson, P., . Oliphant, T.E., 2020. Array programming with NumPy. Nature 585, 357-362. https://doi.org/10.1038/s41586-020-2649-2.
- Hunter, J.D., 2007. Matplotlib: a 2D graphics environment. IEEE Ann. Hist. Comput. 9 (3), 90-95. https://doi.org/10.1109/MCSE.2007.55.
- lezzi, A.M., Fee, D., Haney, M.M., Lyons, J.J., 2020. Seismo-acoustic characterization of mount cleveland volcano explosions. Front. Earth Sci. 8 (573368). https://doi.org/ 10.3389/feart.2020.573368.
- Johnson, J.B., Malone, S.D., 2007. Ground-coupled acoustic airwaves from Mount St. Helens provide constraints on the May 18, 1980 eruption. Earth Planet, Sci. Lett. 258 (1-2), 16-31. https://doi.org/10.1016/j.epsl.2007.03.001.
- Lengliné, O., Duputel, Z., Ferrazzini, V., 2016. Uncovering the hidden signature of a magmatic recharge at Piton de la Fournaise volcano using small earthquakes. Geophys. Res. Lett. 43 (9), 4255-4262. https://doi.org/10.1002/2016GL068383.

- Lesage, P., Heap, M.I., Kushnir, A., 2018. A generic model for the shallow velocity structure of volcanoes. J. Volcanol. Geotherm. Res. 356 (1), 114–126. https://doi.org/10.1016/j. jvolgeores.2018.03.003.
- Matoza R.S. Fee, D. 2014. Infrasonic component of volcano-seismic eruption tremor Geophys. Res. Lett. 41 (6), 1964–1970. https://doi.org/10.1002/2014GL059301.
- Matoza, R.S., Fee, D., 2018. The inaudible rumble of volcanic eruptions, Acoust, Today 14 (1), 17–25. https://acousticstoday.org/issues/2018AT/Spring2018/. Matoza, R.S., Chouet, B.A., Dawson, P.B., Shearer, P.M., Haney, M.M., Waite, G.P., Moran,
- S.C., Mikesell, T.D., 2015. Source mechanism of small long-period events at Mount St. Helens in July 2005 using template matching, phase-weighted stacking, and fullwaveform inversion. J. Geophys. Res. Solid Earth 120 (9), 6351–6364. https://doi. org/10 1002/2015IB012279
- Matoza, R.S., Fee, D., Green, D.N., Le Pichon, A., Vergoz, J., Haney, M.M., Mikesell, T.D., Franco, L., Valderrama, O.A., Kelley, M.R., McKee, K., Ceranna, L., 2018. Local, regional, and remote seismo-acoustic observations of the April 2015 VEI 4 eruption of Calbuco Volcano, Chile. J. Geophys. Res. Solid Earth 123 (5), 3814–3827. https://doi.org/10. 1002/2017IB015182
- Matoza, R., Arciniega-Ceballos, A., 2017. Popocatépetl volcano temporary deployment, 2017-2018 [Data set]. Int. Feder. Digit. Seismogr. Network https://doi.org/10.7914/ SN/5K 2017
- Matoza, R.S., Arciniega-Ceballos, A., Sanderson, R.W., Mendo-Pérez, G., Rosado-Fuentes, A., Chouet, B.A., 2019a. High-broadband seismoacoustic signature of vulcanian explosions at Popocatépetl Volcano, Mexico. Geophys. Res. Lett. 46 (1), 148-157. https:// doi.org/10.1029/2018GL080802.
- Matoza, R., Fee, D., Green, D., Mialle, P., 2019b. Volcano infrasound and the international monitoring system. In: Le Pichon, A., Blanc, E., Hauchecorne, A. (Eds.), Infrasound Monitoring for Atmospheric Studies. Springer, Cham, pp. 1023-1077 https://doi. org/10.1007/978-3-319-75140-5 33.
- McNutt, S.R., 2000. Seismic monitoring. In: Sigurdsson, E., Houghton, B., McNutt, S.R., Rymer, H., Stix, J. (Eds.), Encyclopedia of Volcanoes. Academic Press, pp. 1095-1999.
- Neuberg, J., Pointer, T., 2000. Effects of volcanic topography on seismic broad-band waveforms. Geophys. J. Int. 143 (1), 239-248. https://doi.org/10.1046/j.1365-246x.2000. 00251 x
- Ripepe, M., Ciliberto, S., Schiava, M.D., 2001. Time constraints for modeling source dynamics of volcanic explosions at Stromboli. J. Geophys. Res. Solid Earth 106 (B5), 8713-8727. https://doi.org/10.1029/2000JB900374.
- Ruiz, M.C., Lees, J.M., Johnson, J.B., 2006. Source constrains of Tungurahua volcano explosion events. Bull. Volcanol. 68, 480-490. https://doi.org/10.1007/s00445-005-0023-8.
- Sánchez-Sesma, F.J., Madariaga, R., Irikura, K., 2001. An approximate elastic twodimensional Green's function for a constant-gradient medium. Geophys. J. Int. 146 (1), 237-248. https://doi.org/10.1046/j.0956-540x.2001.01447.x.
- Shelly, D., Hill, D.P., 2011. Migrating swarms of brittle-failure earthquakes in the lower crust beneath Mammoth Mountain, California. Geophys. Res. Lett. 38 (20). https:// doi.org/10.1029/2011GL049336.
- Shelly, D.R., Beroza, G.C., Ide, S., 2007. Non-volcanic tremor and low-frequency earthquake swarms. Nature 446, 305-307. https://doi.org/10.1038/nature05666
- Skoumal, R.J., Brudzinski, M.R., Currie, B.S., 2015. Distinguishing induced seismicity from natural seismicity in Ohio: demonstrating the utility of waveform template matching. J. Geophys. Res. Solid Earth 120 (9), 6284–6296. https://doi.org/10.1002/ 2015|B012265.
- Smith, C.M., McNutt, S.R., Thompson, G., 2016. Ground-coupled airwaves at Pavlof Volcano, Alaska, and their potential for eruption monitoring. Bull. Volcanol. 78 (52). https://doi.org/10.1007/s00445-016-1045-0.
- SSN, 2017. Servicio Sismológico Nacional. Instituto de Geofísica, Universidad Nacional Autónoma de México, México.
- Stephens, C.D., Chouet, B.A., 2001. Evolution of the December 14, 1998 precursory longperiod event swarm at Redoubt Volcano, Alaska. J. Volcanol. Geotherm. Res. 109 (1-3), 133-148. https://doi.org/10.1016/S0377-0273(00)00308-5.
- Tameguri, T., Iguchi, M., Ishihara, K., 2002. Mechanism of explosive eruptions from moment tensor analyses of explosion earthquakes at Sakurajima Volcano, Japan. Bull. Volcanol. Soc.Japan 47 (4), 197-215. https://doi.org/10.18940/kazan.47.4_197.
- Valdes, C., Gonzalez, G., Arciniega, A., Nava, E., Santoyo, M., 1995. Sismicidad del Volcán Popocatépetl a partir del 21 de Diciembre de 1994 al 30 de Marzo de 1995. In: Comité Científico Asesor CENAPRED-UNAM (Ed.), Volcán Popocatépetl: Estudios Realizados Durante la Crisis de 1994-1995. CENAPRED, UNAM, pp. 129-138.
- Virtanen, P., Gommers, R., Oliphant, T.E., Haberland, M., Reddy, T.R., Cournapeau, D., Burovski, E., Peterson, P., Weckesser, W., Bright, J., van der Walt, S.J., Brett, M., Wilson, J., Millman, K.J., Mayorov, N., Nelson, A.R.J., Jones, E., Kern, R., Larson, E., ... SciPy 1.0 Contributors, 2020. SciPy 1.0: fundamental algorithms for scientific computing in Python. Nat. Methods 17 (3), 261-272. https://doi.org/10.1038/s41592-019-0686-2
- Wessel, P., Smith, W.H.F., 1991. Free software helps map and display data. EOS Trans. Am. Geophys. Union 72 (41), 445–446. https://doi.org/10.1029/90E000319.
- Yamada, T., Aoyama, H., Nishimura, T., Hiroshi, Y., Nakamichi, H., Oikawa, J., Iguchi, M., Hendrasto, M., Suparman, Y., 2016. Initial phases of explosion earthquakes accompanying Vulcanian eruptions at Lokon - Empung volcano, Indonesia. J. Volcanol. Geotherm. Res. 327, 310–321. https://doi.org/10.1016/j.jvolgeores.2016.08.011.
 Zobin, V.M., Reyes, G.A., Guevara, E., Bretón, M., 2009. Scaling relationship for Vulcanian
- explosions derived from broadband seismic signals. J. Geophys. Res. Solid Earth 114 (B3). https://doi.org/10.1029/2008JB005983.